Article

Effect of Nb^{5+} and In^{3+} Ions on Moisture Sensitivity of Electrospun Titanium/Tungsten Oxide Nanostructures: Microstructural Characterization and Electrical Response

Georgenes M. G. Silva [1,2], Victor N. S. Leão [1], Michel F. G. Pereira [1], Pedro M. Faia [3] and Evando S. Araújo [1,*]

1 Research Group on Electrospinning and Nanotechnology Applications, Department of Materials Science, Federal University of San Francisco Valley, Juazeiro 48902-300, Brazil; georgenes.gil@ifsertao-pe.edu.br (G.M.G.S.); victornsleao@gmail.com (V.N.S.L.); michelgalvao2014@gmail.com (M.F.G.P.)
2 Federal Institute of Education, Science and Technology of the Sertão Pernambucano, Petrolina 56314-520, Brazil
3 CEMMPRE–Electrical and Computer Engineering Department, University of Coimbra, FCTUC, Polo 2, Pinhal de Marrocos, 3030-290 Coimbra, Portugal; faia@deec.uc.pt
* Correspondence: evando.araujo@univasf.edu.br; Tel.: +55-74-2102-7645

Abstract: In this work, Nb^{5+} and In^{3+} ions were used as dopants in titanium/tungsten oxide nanostructures that are produced by the electrospinning and sintering process, for relative humidity (RH) detection. The microstructural properties were investigated by SEM, EDS, XRD, Raman and FTIR techniques. The electrical response characterization of the samples was performed by electrical impedance spectroscopy in the range of 400 Hz to 40 MHz, at 20 °C. The sensors sensitivity to moisture was evaluated in terms of the impedance variations to RH (10–100%). The combined analysis of the microstructural characterization results confirmed the surface interaction between the oxides and the ions incorporation in *Ti* crystal lattice. All the studied sensors showed a conduction transition from p- to n-type at around 30–40% RH: besides, they also displayed better sensitivity to moisture than those obtained in a previous work using titanium/tungsten combination using a different fabricationn route. The impedance modulus variation up to 1.1 and 1.3 orders of magnitude for the 4 wt % niobium and indium doped samples, respectively. The results are directly associated with the microstructure and alternative preparation process.

Keywords: characterization; preparation; electrospinning; mixed metal oxide; nanostructures

1. Introduction

Humidity is an extremely important parameter for several industrial sectors. The treatment, production and storage of products are some of the processes that require monitoring and adjustments for the relative humidity (RH) of the environment.

Metal oxide semiconductor nanomaterials have recently started to receive increasing attention regarding the production of moisture sensors with better performance, due to their high surface area and excellent chemical, structural and environmental stability [1,2]. In these materials, the electrical response to moisture is associated with the chemisorbed and physiosorbed layers of water molecules on their surface, and with the capillary condensation of water in the porous microstructure [2,3].

Metal oxides can form nanocomposites with other oxides (mixed metal oxides, MMO) and other functional materials, such as conducting polymers and carbon-based materials, in order to ensure higher surface area, less electron-hole recombination and better performance in adsorption, photocatalysis and gas sensing applications [4–7].

MMO nanostructures are notable for the possibility of improving their electrical response to humidity, due to better microstructural and electrical properties, which results from the atomic and surface interaction between the constituent oxides and moisture, when

compared to the individual use of these semiconductors. The selective composition, doping and preparation processes of these materials, are significant factors to obtain nanostructures with high surface area/volume ratio for moisture sensitive applications [4,8].

The combined use of titanium dioxide (TiO_2) and tungsten trioxide (WO_3) with selective dopants such as Zn^{2+}, Cu^{2+}, Nb^{5+} and V^{5+} ions, in volumetric pellets arrangement, has been studied for the development of more efficient MMO sensors [9–11]. While WO_3 interacts superficially with TiO_2, which increases both the thermal/structural stability and the conductivity of the system, the dopants increase the degree of adsorption of water molecules, resulting in an excellent sensitivity to RH variations.

Recently, TiO_2/WO_3 MMO have been produced by electrospinning and sintering processes [12,13]. With this preparation route, the oxides are first encapsulated in polymeric micro/nanofibers and then sintered to obtain a uniform dispersion of the sensor material on the interdigitated electrodes. This alternative method ensures the formation of MMO porous films in detriment of volumetric pellets in the detection of moisture, simplifying fabrication route and maintaining sensing quality with a considerably smaller amount of material, a significant step in the miniaturization direction of the devices [12,14].

In this work, authors study the effect of the introduction of Nb^{5+} and In^{3+} doping ions on moisture sensitivity of TiO_2/WO_3 mixed metal oxides, produced by electrospinning and sintering. The microstructure of the produced materials was investigated and directly related to the RH-dependent impedance (Z) variations.

2. Materials and Methods

2.1. Materials

Anatase titanium dioxide (TiO_2), monoclinic tungsten trioxide (WO_3), niobium pentoxide (Nb_2O_5), indium (III) oxide (In_2O_3) (metal oxides were purchased from Sigma Aldrich), poly (methacrylic acid, methyl methacrylate), 1:1 (Evonik Industries), and ethyl alcohol PA (99.8%) (Neon) were used as received.

2.2. Sample Preparation

The sensors were prepared in two steps: (i) Electrospinning of the polymer solution (containing the metal oxides); and (ii) sintering of the resulting materials from the first step.

The polymer solution for the electrospinning process was prepared from 2.0 g of polymer in 8 mL of ethyl alcohol. The mixed metal oxides (MMO) compositions were obtained from mixtures between TiO_2 and WO_3 (1:1 mole ratio) with 2, 4 and 6 wt % of Nb_2O_5 ($TW - Nb2$, $-Nb4$ and $-Nb6$ samples), and In_2O_3 ($TW - In2$, $-In4$ and $-In6$ samples) dopants, respectively.

The samples (0.25 g of each metal oxide composition solubilized in 2 mL of polymer solution) were transferred to a conventional syringe (10 mL capacity and 0.7 mm diameter of the metal capillary), and kept at a constant pressure.

A 100 µL min^{-1} flow rate of the solutions was established at the capillary tip, with an electrical differential voltage potential of 16 kV applied between the needle and a grounded 10 cm × 10 cm plane metal collector, 10 cm apart. The produced fibers (containing the oxides) were deposited over a pair of gold (Au) interdigitated electrical electrodes (1.1 cm × 1.1 cm) placed on an insulating alumina substrate. All experiments were carried out at room temperature (20 °C).

In sequence, each sample was sintered in an oven at 500 °C for 2 h, in order to eliminate the organic matrix and obtain the metal oxide films for moisture sensing tests. Figure 1 illustrates the samples preparation steps for the analysis of their electrical responses to RH.
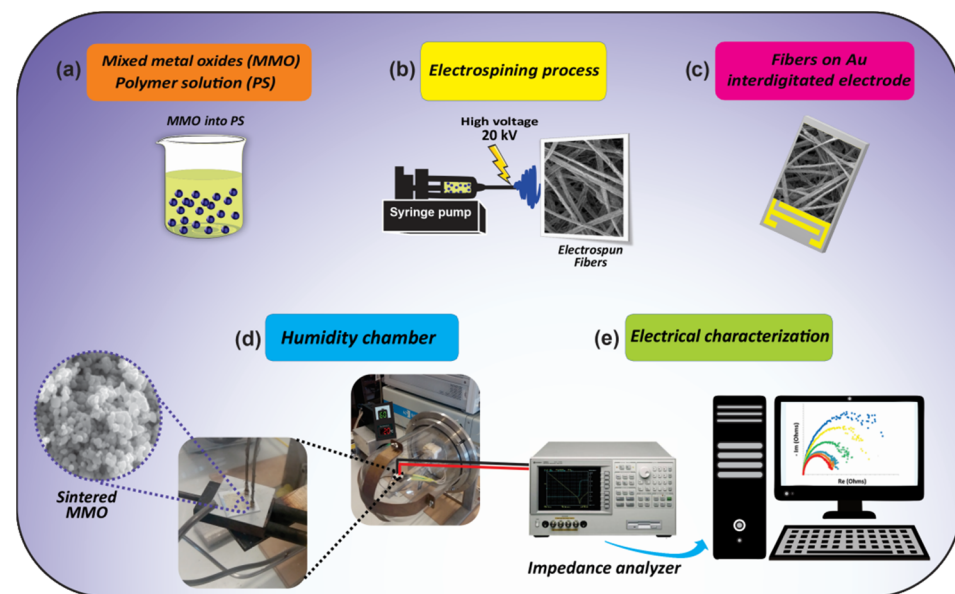
Figure 1. Illustration of the samples preparation for moisture sensing tests: (**a**) Polymeric solution containing the mixed metal oxides (MMO) for the (**b**) electrospinning process; (**c**) deposition of the electrospun fibers (containing the oxides) on the Au interdigitated electrode; (**d**) sintered oxides for electrical tests in the humidity chamber; (**e**) RH dependent electrical response.

2.3. Microstructural Characterization

The materials microstructure was analyzed by: (i) scanning electron microscopy. SEM (Vega 3XM (Tescan, Brno, Czech Republic), equipped with an energy-dispersive X-ray detector, EDX, with 10–20 kV accelerating voltage); (ii) Raman spectroscopy, laser wavelength, λ, of 532 nm, 20–25 mW (HORIBA Scientific, Osaka, Japan); (iii) Fourier transform infrared spectroscopy, FTIR (Schimadzu Prestige 21 equipment (Shimadzu Corporation, Kyoto, Japan), KBr pellet); (iv) X-ray diffraction. XRD (Miniflex Rigaku equipment (Rigaku Corporation, Tokyo, Japan), Cu Kα radiation, $\lambda = 1.54056$ Å, 40 kV voltage, 15 mA current, scan rate of $0.02°\cdot s^{-1}$, 15–70° 2θ range). X-Pert HighScore software was used to identify the crystalline phases. Crystallographic data were obtained from the International Center for Diffraction Data (ICDD).

2.4. Electrical Response

The systems electrical response to relative humidity, RH, exposure was investigated by electrical impedance spectroscopy (impedance analyzer HP4194A (Hewlett-Packard, Santa Clara, CA, USA), in the frequency range from 400 Hz to 40 MHz. The samples were tested in a humidity chamber (humidity and temperature automatically controlled, with an error smaller than ± 1%), see Figure 1d), with RH values ranging from 10 to 100%, at 20 °C. The sensitivity of the systems to RH variations was assessed in terms of the variation of their impedance module values $|Z|$ ($|Z| = \sqrt{(\text{Re } Z)^2 + (\text{Im } Z)^2}$), where Re Z and Im Z are the resistance and the reactance of the measured impedance by impedance spectroscopy).

2.5. Statistical Analysis

Fiber diameter, grain size of the sintered structures and their electrical response were given as the average of three independent measurements, for each tested oxide composition. Inferential statistical analyzes (normality and equality of means tests) were performed with 95% confidence level (or significance level, α, of 0.05) and compared to the p-value returned by these tests. For p-value $> \alpha$, the normality and equality of means hypotheses are accepted. Diameter and grain size values were obtained from SEM micrographs using ImageJ software.

3. Results and Discussion

3.1. Microstructural Analysis

The morphological aspects of the oxides-containing electrospun fibers and the sintered MMO were investigated from the micrographs obtained by SEM. Figure 2 presents SEM images of the produced fibers (preliminary material for the preparation of nanostructures for moisture detection) and their respective EDX mappings.
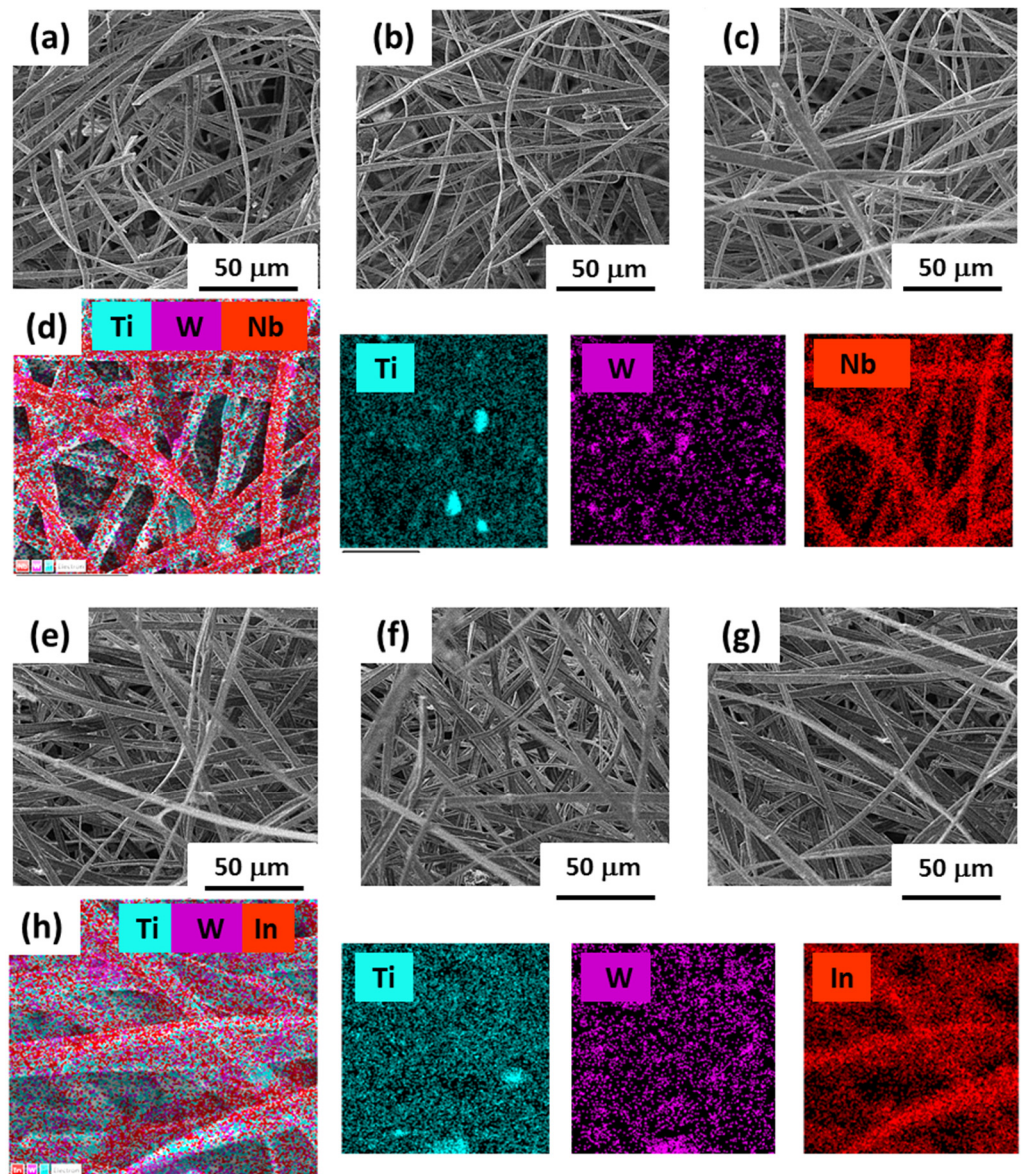

Figure 2. SEM images of electrospun fibers containing $TW - Nb$ MMO with (**a**) 2, (**b**) 4 and (**c**) 6 wt % of Nb_2O_5 and $TW - In$ MMO with (**e**) 2, (**f**) 4 and (**g**) 6 wt % of In_2O_3; and EDX mappings of (**d**) $TW - Nb4$ and (**h**) $TW - In4$, respectively.

All fibers with $TiW - Nb$ and $TiW - In$ compositions exhibited regular diameters and showed no surface structural defects (e.g., beads) [15]. In addition, it was found that fiber size follows a normal distribution (p-value $> \alpha$), with mean diameters of $5.6 \pm 2.1 \ \mu m$ (sample size (n) = 61), $5.4 \pm 2.3 \ \mu m$ (n = 51) and $6.5 \pm 2.8 \ \mu m$ (n = 69) for the $TiW - Nb2$, $-Nb4$ and $-Nb6$, and $6.1 \pm 1.7 \ \mu m$ (n = 49), $5.7 \pm 2.9 \ \mu m$ (n = 67) and $5.9 \pm 2.0 \ \mu m$ (n = 63) for the $TiW - In2$, $-In4$ and $-In6$ models, respectively. The hypothesis tests on the population mean difference, with unknown standard deviation, confirmed that all

produced fibers have similar diameters, with no statistically significant differences. The constant diameter of the fibers observed even with increasing concentration of dopants, is an important factor allowing to relate moisture sensitivity of the sintered material only with the interaction between the oxides, in each tested configuration.

Representative energy-dispersive X-ray (EDX) maps of $TW - Nb$ and $TW - In$ MMO-loaded fibers confirmed that the populations of metallic elements that compose the semiconductor matrix (*Ti* and *W*) and the doping elements (*Nb* and *In*) have uniform distribution in all electrospun samples, as shown for the $TW - Nb4$ and $TW - In4$ samples (Figure 2d,h, respectively). In other words, the fibers act as a polymeric mold to promote the suitable distribution of the materials on the electrode and prevent further aggregation of the oxide particles. These results reveal that electrospinning can be used as an effective and low-cost alternative fabrication process (compared to usual methods, such as vapor deposition, coating, and sputtering techniques, among others [16]): Consequently, materials with expectable higher surface area to volume ratio can be produced, which directly affect the sensing response of the oxide films that result from sintering. It is know that the adsorption of water vapor on the materials' surfaces is promoted by a higher contact surface area, due to its porous nature, which affects the electrical conduction. This change encompasses the resistance, capacitance or electrolytic conduction depending on the sensor type [17]. After sintering at 500 °C, it is possible to observe the morphological differences of the final materials that will be used for moisture detection (Figure 3).
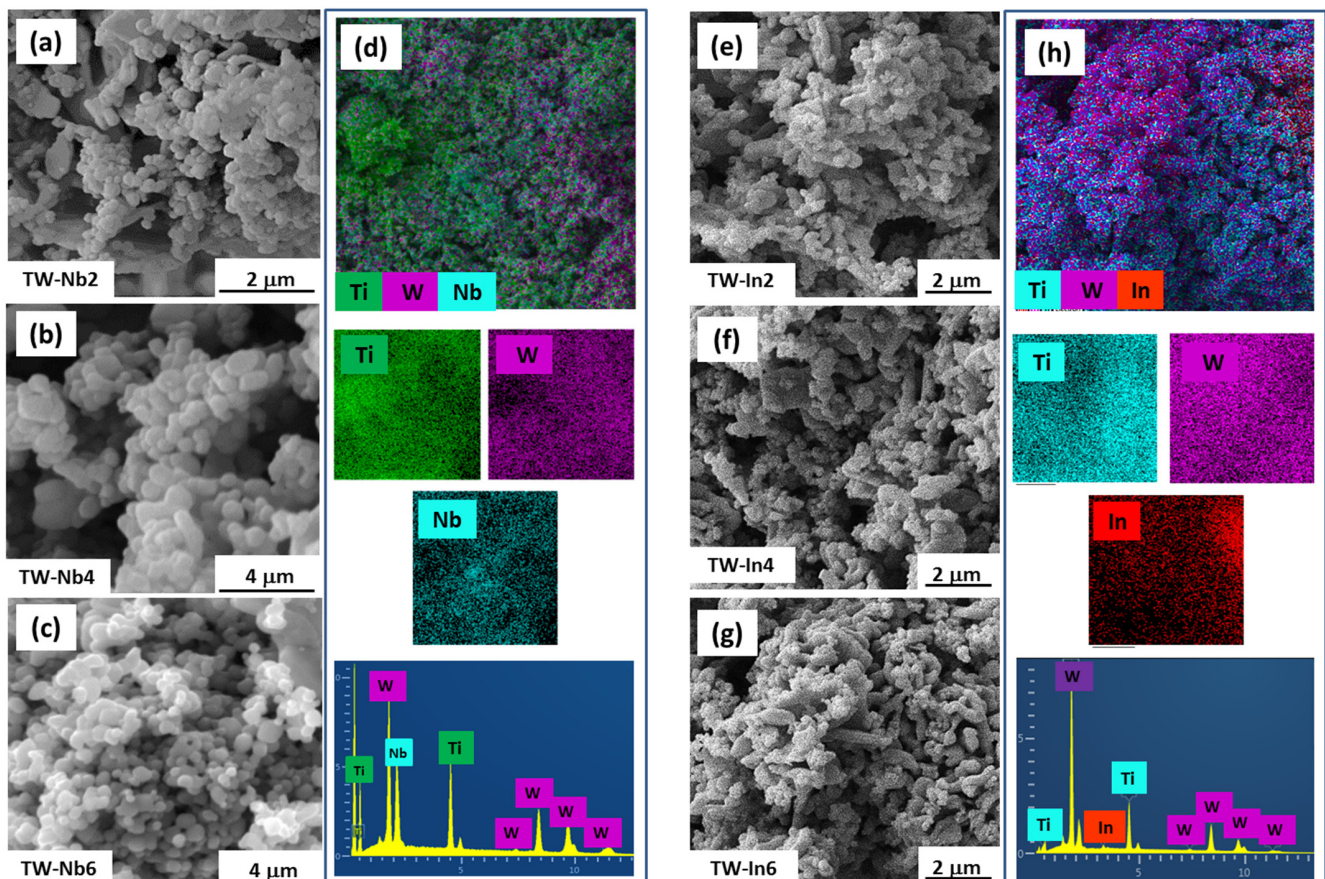

Figure 3. SEM images of *Nb*-doped (**a**) $TW - Nb2$, (**b**) $TW - Nb4$ and (**c**) $TW - Nb6$ and *In* -doped (**e**) $TW - In2$, (**f**) $TW - In4$ and (**g**) $TW - In6$ sintered MMO; EDX elemental composition and mapping of (**d**) $TW - Nb4$ and (**h**) $TW - In4$ sensors.

EDX elemental composition and mapping, Figure 3d,h, confirmed the presence and continuity of the regular distribution of *Ti* and *W* base metals and of *Nb* and *In* dopants

in the sintered samples, as exemplified in $TW - Nb4$ and $TW - In4$ samples (Figure 3d,h, respectively).

In addition, Figure 3a–c,e–g present micrographs of the produced MMO. The images show materials with a porous structure and particles with dimension on the order of 100 to 400 nm, without the polymeric material. It is possible to observe that the systems produced with 2, 4 and 6 wt % niobium and 2 and 4 wt % indium have mostly spherical particles, which optimizes the application of these structures for moisture sensing. The average diameter of these particles was estimated to be 159.3 ± 48.5 nm ($n = 141$), 168.3 ± 54.3 nm ($n = 128$) and 189.9 ± 84.9 nm ($n = 103$), for $TW - Nb2$, $TW - Nb4$ and $TW - Nb6$ samples, and of 167.5 ± 34.1 nm ($n = 161$) and 178.3 ± 69.8 nm ($n = 149$) for $TW - In2$ and $TW - In4$ ones, respectively. Statistical analysis of grain size proved that there are no significant differences in particle size among the different fabricated systems. It is important to emphasize that these registered characteristics are essential for moisture sensing applications, which favor the adsorption processes of water molecules from the environment, on the semiconductors surface and porous structure. The $TW - In6$ sample showed more elongated particles, with an average diameter of the order of 280.5 ± 100.2 nm ($n = 77$), as a result of the seen nanoparticles agglutination.

Based on the micrographs discussion, the assumption made above about the obtention of samples with higher surface area is greatly supported. Indeed, by looking at the micrographs, authors can state that the samples exhibit high porosity, particularly the ones with lower content of Indium and Niobium where higher voids between agglomerates are visible, which is a clear indication of the existence of high contact surface area.

FTIR obtained spectra for all samples, Figure 4a, demonstrates the absence of molecular vibration bands from the polymer (in the wavenumber range of 1000 to 3600 cm^{-1} [18]), which proves the previous indication that the polymeric mold was completely removed. Furthermore, a wide band in the range of 400–800 cm^{-1} was noted as the typical signature of the metal oxides presence in the sintered samples. This proves that the sensing interactions take place in the organic matter-free MMO nanostructures, as projected.
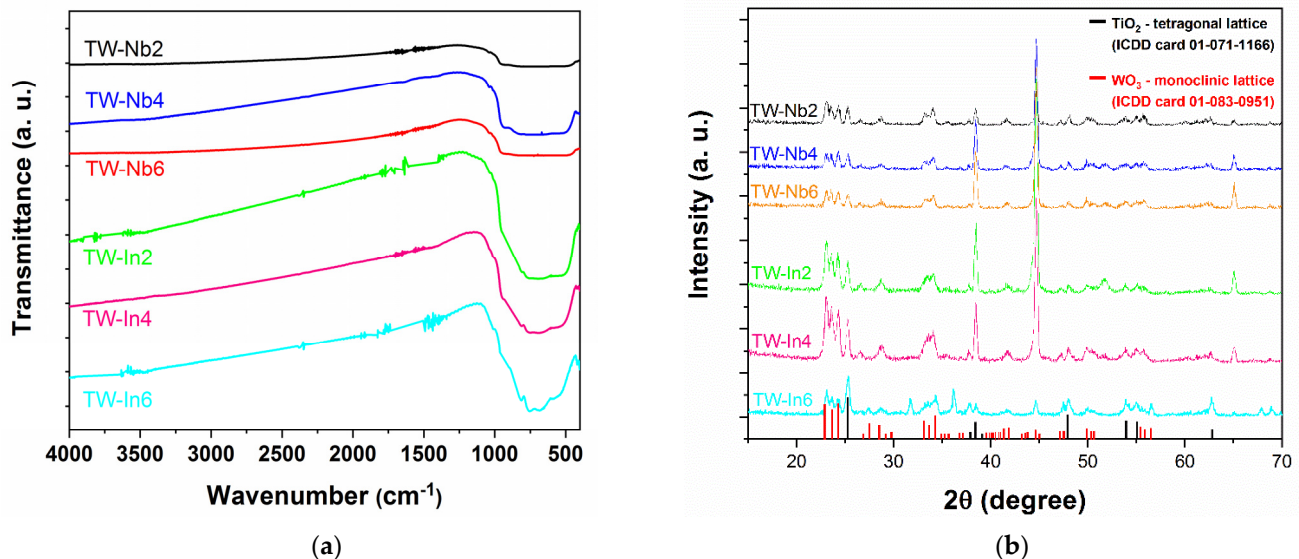

Figure 4. (**a**) FTIR spectra and (**b**) XRD patterns of all $TW - Nb$ and $TW - In$ sintered MMO, varying dopant concentrations.

The X-ray diffractograms of the sintered TW-Nb and TW-In MMOs are presented in Figure 4b.

The results show that all produced MMO are composed of titanium dioxide in the anatase phase, with tetragonal crystal structure (space group D_{4h}^{19} $I4_1/amd$, ICDD card #01 − 071 − 1166), and tungsten trioxide, with monoclinic crystalline system (a = 7.306, b = 7.540, c = 7.692, $\alpha = \gamma = 90°$ and $\beta = 90.88°$, space group $P2_1/c$, ICDD card #01 −

083 − 0951). This shows that the sintering process of TiO_2 (combined with WO_3, at 500 °C) causes no phase change or solid solution formation from these oxides [19].

The lattice parameters for TiO_2 in TW MMO are $a = b = 3.785$ Å and $c = 9.514$ Å, $\alpha = \beta = \gamma = 90°$ [13]. However, it is possible to notice the dependence of TiO_2 lattice parameters with Nb and In concentrations in each sample (Table 1).

Table 1. Lattice parameters of TiO_2 in $TW − Nb$ and $TW − In$ mixed metal oxides (MMO).

Lattice Parameters		
MMO	**$a = b$**	**c**
$TW − Nb2$	3.781	9.527
$TW − Nb4$	3.739	9.638
$TW − Nb6$	3.720	9.722
$TW − In2$	3.782	9.525
$TW − In4$	3.751	9.585
$TW − In6$	3.752	9.580

In $TW − Nb$ samples, a progressive decrease in a and b values and an increase in the value of the c parameter is noted (from 2 to 6 wt % of Nb_2O_5), which indicates an increase in volume of the TiO_2 unit cell. The same behavior is obtained for $TW − In2$ and $−In4$ samples, while the $−In6$ model shows no significant changes in the crystal parameters (related to $−In4$ configuration).

In addition, once known that the doping materials have a well-defined crystal structure, and that they were not detected in the XRD diffraction spectra of all $TW − Nb$ and in $TW−(In2$ and $In4)$ samples, there is an indication that the Nb^{5+} and In^{3+} ions (ionic radius close to Ti^{4+} with 0.74, and 0.80 Å, respectively [20,21]) are effectively acting as dopants in the TiO_2 crystal structure, occupying the vacancies of the Ti atom sites [22].

The invariance of the lattice parameters in the $TW − In6$ sample and the appearance of In_2O_3 characteristic peaks in their XRD spectrum, at $2θ = 31.3°$, $36.1°$ and $61.9°$, indicate that a greater fraction of the indium concentration does not interact at atomic level and promotes interaction on the surface of the MMO. This property can influence the size and shape of the grains, porosity and physical properties (conductivity, surface area, among others) of the final material, as verified for the morphology of this sample obtained by SEM images (Figure 3g).

The Raman spectra of the nanocomposites are shown in Figure 5. For comparison, the spectrum of pure anatase TiO_2 nanoparticles sintered at 500 °C was also analyzed. The sample presented the characteristic molecular vibration bands of the anatase at 145, 198, 393, 514 and 637 cm^{-1} wavenumbers, as described in the literature [23].

In $TW − Nb$ and $TW − In$ samples, the TiO_2 bands were also observed, but all of them were displaced to regions with a lower wavenumber value. For all samples, except for the $TW − In4$ model, these shifts were in the order of 8 to 12 cm^{-1}. For the sample with 4 wt % of indium, this alteration also occurred but with a greater wavenumber variation (16 to 20 cm^{-1} range, when compared to the values obtained for the anatase TiO_2. The vibrational bands signature of monoclinic WO_3 was also verified in niobium and indium-doped nanocomposites at 263, 316, 707 and 799 cm^{-1} wavenumbers [10,24]. In the TW-In4 sample, the characteristic WO_3 bands were also found shifted to smaller wave numbers, by approximately 9 cm^{-1}.

These Raman band changes to regions of the spectrum with lower wavenumbers is known as redshift. This phenomenon is associated with distortions in the atomic structure of TiO_2, as well as the processes of surface relaxation and phonon confinement, which favor the electrical response of these systems to RH variations [25]. Therefore, the occurrence of redshift demonstrates that a portion Nb^{5+} and In^{3+} ions concentration was introduced in the available vacancies of Ti atoms in the TiO_2 crystal lattice, since the ionic radius of the dopants are close to that of titanium.

The combined analysis of SEM micrographs and XRD and Raman spectra showed that the planned nanocomposites were successfully produced for testing the electrical response of systems to RH variations.
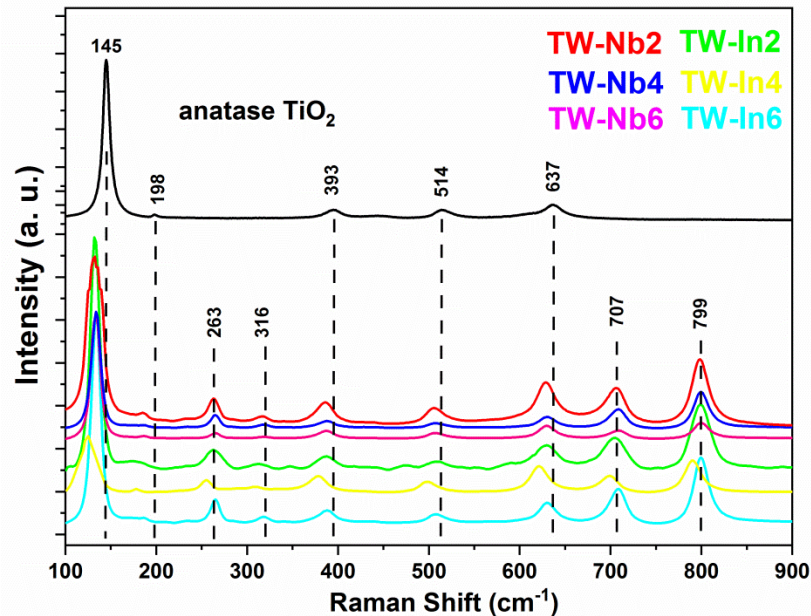

Figure 5. Raman spectra of the $TW - Nb$ and $TW - In$ MMO nanocomposites and pristine anatase TiO_2 nanoparticles.

3.2. Electrical Response

The electrical response of TW-Nb and TW-In mixed metal oxides to RH variations was investigated by electrical impedance spectroscopy. The $TW - Nb$ and $TW - In$ MMO electrical response to moisture are dependent on the adsorption processes (chemisorption and physisorption) of water from the environment on the surface, and porous structure, of these nanostructures (Figure 6a).

Chemisorption is characterized by the first adsorbed layer of water molecules covering the oxides surface and porous open structure. This layer is usually completely adsorbed at around 30 to 40% RH concentration, and will be strongly bonded to the oxides, without further influence of further RH variations. With the progressive increase in relative humidity, physiosorbed layers begin to form over the chemisorbed layer, one after the other. In contrast with the first case, these layers are unstable and can be easily removed with increasing temperature or decreasing RH concentration in the atmosphere [26,27].

With water saturation on the MMO surface, water molecules begin to condense in the microscopic pores between the grains, in the bulk of the sensor material. In this context, the accumulation of electrical charge carriers in the barrier between the grains contributes to electrical polarization (from the movement of these charges as a result of an applied electrical field) [19,28].

As RH increases, the minimum value in the total conductance is noted for all tested samples. Figure 7 shows this characteristic Nyquist plots (imaginary versus real parts of the impedance, −Im Z vs. Re Z) for the $TW - Nb$ samples as a RH function.

This phenomenon is a signature of a p- to n-type conduction transition in materials [29–32]. P-type conduction is noted at low RH concentrations in the region where the chemosorbed layer is formed (know has low humidity range, below 30–40% RH: form RH values above the 40% lays the called high humidity range). In this case, oxygen from the humidified air at room temperature can be adsorbed in the form of O^-, O^{2-}, O_2^- and O_2^{2-} ions. This causes the density of free electrons to decrease. Consequently, the electrical impedance of the material increases due to the removal of charge carriers from

the conduction band. In this configuration, oxide ion species also react with humidity molecules from the medium and the materials conduction band becomes again occupied by electrons.

Therefore, the total conductivity in the material is dependent on the rate at which these reactions occur. The production of MMO sensor films by electrospinning results in nanostructured systems with a high surface area to volume ratio. As a consequence, p-type conduction is dominant in the low RH range. However, when the RH of the environment is around 40%, the type of conduction in the material is inverted (p-type to n-type) due to the greater electrons availability in the conduction band. The impedance of these systems continues to decrease progressively with the formation of the first and following physiosorbed layers, mainly due to the transport and electrical polarization mechanisms, especially the hopping conduction of H^+ protons.

The increase in physisorption controlled conduction mechanisms (due to the increase in RH in the environment) evidences the presence of hydronium (H_3O^+) ions for the formation of a high density of H^+ protons as charge carriers, by the Grotthuss mechanism [33], Figure 6b). In this configuration, the instability of the hydronium chemical bond promotes the hopping transfer of a H^+ proton to the nearest water molecule. As a result, the H_2O molecules are ionized and form another H_3O^+ ion. This process is repeated on the surfaces of the sensors while the RH of the environment is kept constant. This same behavior is observed for the $TW - In$ models (the detailed description of the RH-dependent impedance variations for these two doped systems will be discussed from the data in Figure 8).
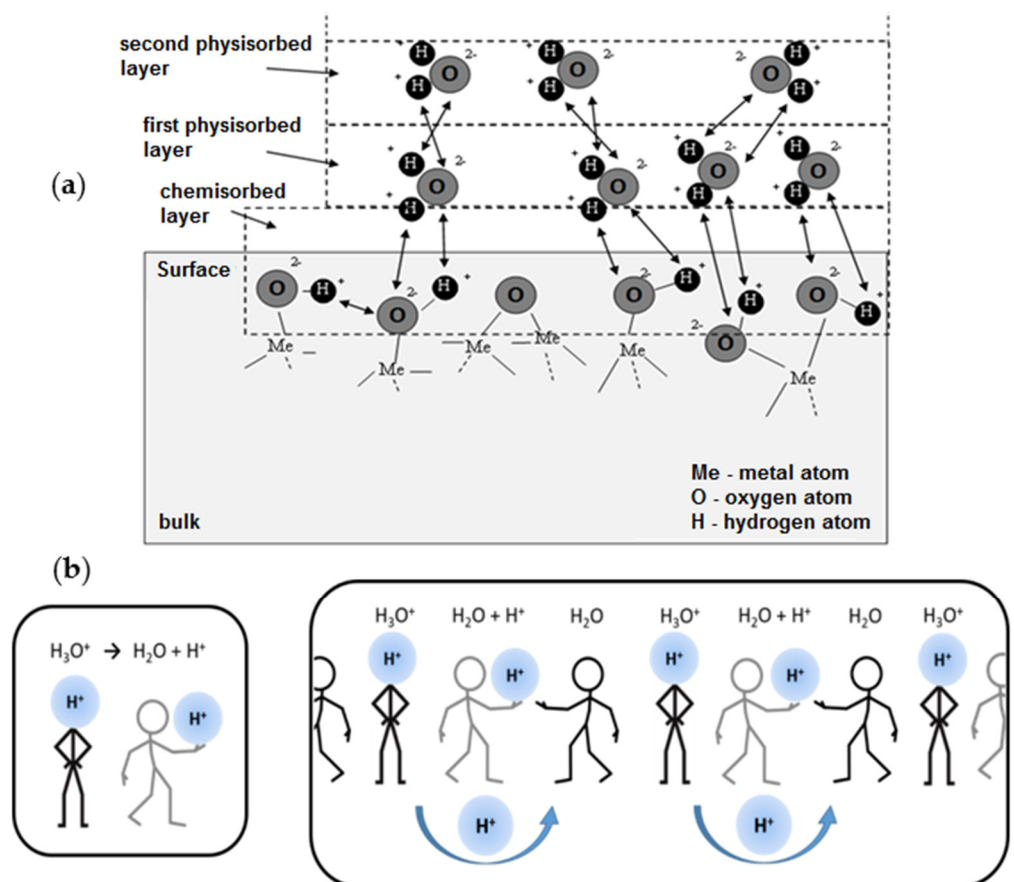

Figure 6. (**a**) Scheme of the chemisorbed and physiosorbed water layers on the oxides surface and (**b**) illustrative representation of the Grotthuss mechanism.
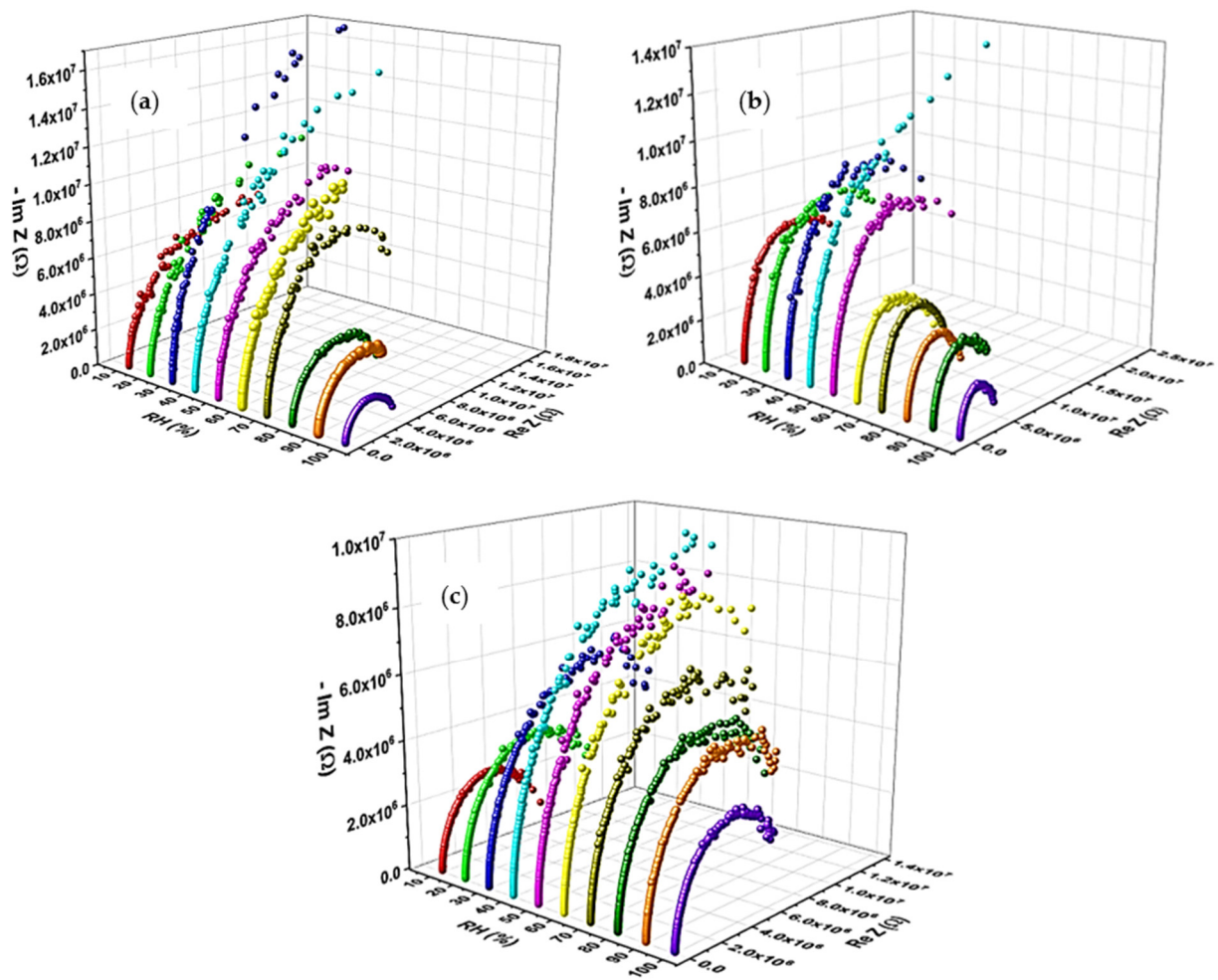
Figure 7. Nyquist Plot of TW-Nb MMO as a function of RH, in the frequency range from 400 Hz to 40 MHz, for the (**a**) *TW − Nb*2, (**b**) *TW − Nb*4 and (**c**) *TW − Nb*6 samples.
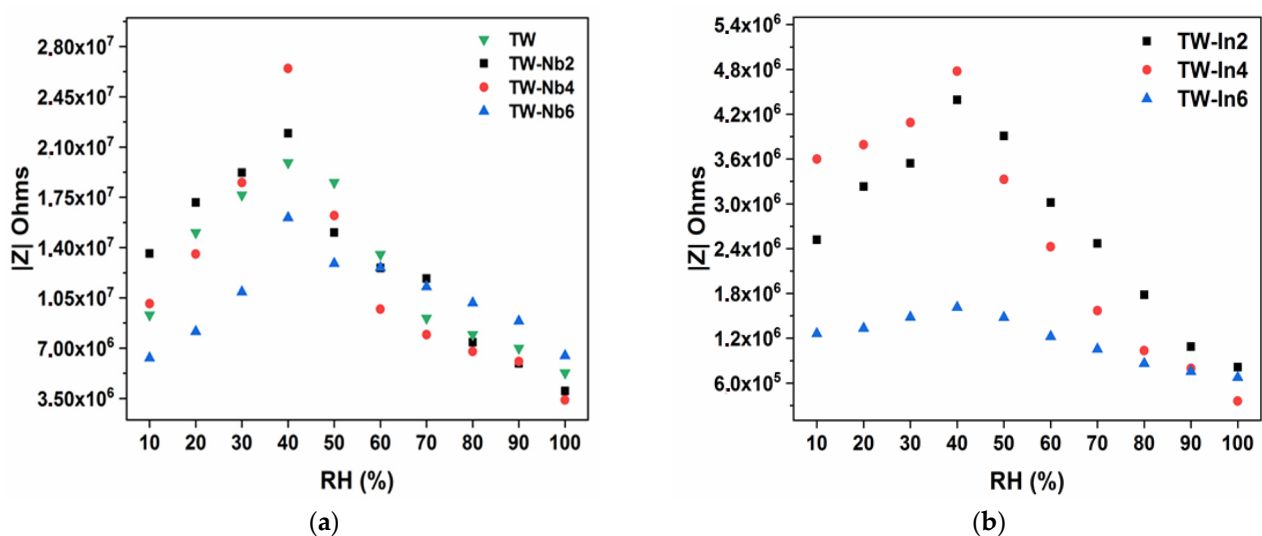

Figure 8. (**a**) Impedance variation with RH for (**a**) *TW − Nb* and (**b**) *TW − In* mixed metal oxides at 1 kHz and 20 °C.

In fact, Nyquist plots for all MMO nanostructures return compressed semicircles, indicating that conduction in these materials is dominated by the relaxation processes at the surface of grains and through grain boundaries [34]. Diffusion process are present, at

least in the interface between the measuring electrodes and the material, but clearly their contribution is insignificant to the overall impedance measured of the sensors. Once it is not predictable by observation of the SEM images of the existence of a significant number of pores in the mesoporous region, no further diffusion contributions are expected (it is known that a large porosity in the mesoporous region, where capillary water condensation and consequently water reactivity are enhanced, and contributes to the materials' overall electrical response).

Figure 8 shows the variations in the impedance modulus obtained for the $TW - Nb$ and $TW - In$ systems as a function of RH, at 40–100% RH range. The $TW - Nb2, -Nb4$ and $-Nb6$ models presented an impedance variation of 0.81, 1.11 and 0.73, in order of magnitude, respectively. In addition, the $TW - In2, -In4$ and $-In6$ samples showed variations of 0.96, 1.27 and 0.45, respectively. The results indicate that the systems tested in this work present better sensitivity to RH variations than those obtained with the TW systems (produced in the form of pellets or prepared by electrospinning, without addition of dopants) [9,13].

The best electrical moisture sensitivity results for niobium and indium-doped samples at 4 wt % are related to the MMO preparation process and the efficiency of Nb^{5+} and In^{3+} ions as dopants in the TiO_2 structure, at this concentration, as confirmed in the XRD and Raman experiments. However, the best candidate for future application in a sensing device is in the authors' opinion the indium doped sample at 2 wt %, as it exhibits both in low and high humidity ranges, almost linear variations to RH changes, with almost the same overall impedance modulus variations than those displayed by the samples doped with niobium and indium at 4 wt %.

The samples with 6 wt % niobium and indium showed a lower impedance excursion with increasing moisture (compared to the other samples). This means that these two systems are more conductive than samples produced with lower concentrations of dopants, due to the greater surface interaction between the oxides, demonstrated in the SEM and XRD experiments. As verified, up to a concentration of 4 wt %, the efficacy of niobium and indium ions can be tested as dopants, in an attempt to produce systems with greater sensitivity to moisture, while at higher concentrations, the sensory quality is strongly reduced.

The electrical response stability to moisture of $TW - Nb$ and $TW - In$ samples was tested at three RH working values (at 50, 70 and 90% RH-after the p-n transition) at 1 kHz, in terms of the relative variation of impedance, over the seven-day measurement interval under constant RH regime, see Table 2, where Z_i and Z_f are the values of $|Z|$ measured at p-n transition and at 100% of relative humidity, respectively. The results showed that all doped samples have small variation in impedance values ($\leq$4.1%), with potential for moisture sensing in applications that depend on RH monitoring, similar to the TW sensors previously produced earlier, without dopants addition [9,13].

Table 2. Electrical response stability to moisture (at 50, 70 and 90% RH) for $TW - Nb$ and $TW - In$ sensors produced with 2, 4 and 6 wt % of Nb_2O_5 and In_2O_3, respectively.

	Nb_2O_5 **(wt %)**			In_2O_3 **(wt %)**		
	2	4	6	2	4	6
RH (%)	Electrical response stability $\left(100 - \frac{Z_i - Z_f}{Z_i}\right)$ (%)					
50	96.1	97.2	98.1	96.7	95.7	96.7
70	95.9	96.9	97.1	96.9	98.3	97.6
90	97.7	97.3	97.3	96.1	97.6	96.8

4. Conclusions

The $TW - Nb$ and $TW - In$ samples were successfully prepared by the alternative fabrication route, by electrospinning and sintering processes. The electrospinning technique proved to be adequate to obtain nanostructures of mixed metal oxides with potential for

RH sensing. The microstructural characterization justified the sensitivity results obtained using Nb^{5+}- and In^{3+}-doped samples, from the impedance variations of the systems.

All tested samples electrically responded to variations in RH range. The best impedance variation results were obtained for doped samples with 4 wt % of niobium and indium. However, the best candidate for future use in a sensing device is the indium doped sample at 2 wt % due to its almost linear electrical response. These systems returned a variation of approximately 1.1, and 1.3 order of magnitude, respectively, which consequently increased the MMO sensitivity to moisture detection. However, samples with 6 wt % of dopants demonstrated to be more conductive than the previous ones, as a consequence of changes in their microstructures, which resulted in less impedance variation during the moisture sensing tests.

Author Contributions: Sample preparation and characterization, writing, editing and review, G.M.G.S., V.N.S.L., M.F.G.P., P.M.F. and E.S.A. All authors have read and agreed to the published version of the manuscript.

Institutional Review Board Statement: Not applicable.

Informed Consent Statement: Not applicable.

Conflicts of Interest: The authors declare no conflict of interest.

References

1. Chavali, M.S.; Nikolova, M.P. Metal oxide nanoparticles and their applications in nanotechnology. *SN Appl. Sci.* **2019**, *1*, 607. [CrossRef]
2. Steele, J.J.; Taschuk, M.T.; Brett, M.J. Nanostructured metal oxide thin films for humidity sensors. *IEEE Sens. J.* **2008**, *8*, 1422–1429. [CrossRef]
3. Chowdhury, N.K.; Bhowmik, B. Micro/nanostructured gas sensors: The physics behind the nanostructure growth, sensing and selectivity mechanisms. *Nanoscale Adv.* **2021**, *3*, 73–93. [CrossRef]
4. Shaheen, K.; Shah, Z.; Khan, B.; Adnan; Omer, M.; Alamzeb, M.; Suo, H. Electrical, photocatalytic, and humidity sensing applications of mixed metal oxide nanocomposites. *ACS Omega* **2020**, *5*, 7271–7279. [CrossRef]
5. Jung, D.; Kim, J.; Lee, G.S. Enhanced humidity-sensing response of metal oxide coated carbon nanotube. *Sens. Actuator. A Phys.* **2015**, *223*, 11–17. [CrossRef]
6. Ansari, M.O.; Ansari, S.A.; Cho, M.H.; Ansari, S.P.; Abdel-wahab, M.S.; Alshahrie, A. Conducting polymer nanocomposites as gas Sensors. In *Functional Polymers*; Jafar, M.M., Sheardown, H., Al-Ahmed, A., Eds.; Springer: New York, NY, USA, 2019; pp. 1–9. [CrossRef]
7. Saqib, M.; Khan, S.A.; Mutee Ur Rehman, H.M.; Yang, Y.; Kim, S.; Rehman, M.M.; Young Kim, W. High-performance humidity sensor based on the graphene flower/zinc oxide composite. *Nanomaterials* **2021**, *11*, 242. [CrossRef] [PubMed]
8. Tripathy, A.; Pramanik, S.; Cho, J.; Santhosh, J.; Abu Osman, N.A. Role of morphological structure, doping, and coating of different materials in the sensing characteristics of humidity sensors. *Sensors* **2014**, *14*, 16343–16422. [CrossRef]
9. Faia, P.M.; Jesus, E.L.; Louro, C.S. TiO_2:WO_3 composite humidity sensors doped with ZnO and CuO investigated by impedance spectroscopy. *Sens. Actuators B Chem.* **2014**, *203*, 340–348. [CrossRef]
10. Faia, P.M.; Libardi, J.; Louro, C.S. Effect of V_2O_5 doping on P- to N-conduction type transition of TiO_2:WO_3 composite humidity sensors. *Sens. Actuators B Chem.* **2016**, *222*, 952–964. [CrossRef]
11. Faia, P.M.; Libardi, J.; Barbosa, I.; Araújo, E.S.; Oliveira, H.P. Preparation, characterization, and evaluation of humidity-dependent electrical properties of undoped and niobium oxide-doped TiO_2:WO_3 mixed powders. *Adv. Mater. Sci. Eng.* **2017**, *2017*, 2808262. [CrossRef]
12. Baghali, M.; Jayathilaka, W.; Ramakrishna, S. The role of electrospun nanomaterials in the future of energy and environment. *Materials* **2021**, *14*, 558. [CrossRef]
13. Araújo, E.S.; Leão, V.N.S. TiO_2/WO_3 heterogeneous structures prepared by electrospinning and sintering steps: Characterization and analysis of the impedance variation to humidity. *Adv. Ceram.* **2019**, *8*, 238–246. [CrossRef]
14. Wang, Y.; Yokota, T.; Someya, T. Electrospun nanofiber-based soft electronics. *NPG Asia Mater.* **2021**, *13*, 22. [CrossRef]

15. Korycka, P.; Mirek, A.; Kramek-Romanowska, K.; Grzeczkowicz, M.; Lewińska, D. Effect of electrospinning process variables on the size of polymer fibers and bead-on-string structures established with a 2^3 factorial design. *Beilstein J. Nanotechnol.* **2018**, *9*, 2466–2478. [CrossRef] [PubMed]

16. Usha, K.S.; Sivakumar, R.; Sanjeeviraja, C. Optical constants and dispersion energy parameters of NiO thin films prepared by radio frequency magnetron sputtering technique. *J. Appl. Phys.* **2013**, *114*, 123501. [CrossRef]

17. Blank, T.A.; Eksperiandova, L.P.; Belikov, K.N. Recent trends of ceramic humidity sensors development: A review. *Sens. Actuators B Chem.* **2016**, *228*, 416–442. [CrossRef]

18. Gulshan, M.; Sai, M.L.S.; Hemalatha, T.; Sri, U.J.; Ramarao, N. Formulation and development of microspheres for the treatment of familial adenomatous polyposis. *Int. J. Appl. Pharm.* **2017**, *9*, 66–72. [CrossRef]

19. Farahani, H.; Wagiran, R.; Hamidon, M.N. Humidity sensors principle, mechanism, and fabrication technologies: A comprehensive review. *Sensors* **2014**, *14*, 7881–7939. [CrossRef]

20. Shannon, R.D. Revised effective ionic radii and systematic studies of interatomic distances in halides and chalcogenides. *Acta Crystallogr. A* **1976**, *32*, 751–767. [CrossRef]

21. Wiglusz, R.J.; Watras, A.; Malecka, M.; Deren, P.J.; Pazik, R. Structure evolution and up-conversion studies of $ZnX_2O_4:Er^{3+}/Yb^{3+}$(X = Al^{3+}, Ga^{3+}, In^{3+}) nanoparticles. *Eur. J. Inorg. Chem.* **2014**, *6*, 109–1101. [CrossRef]

22. Wojcieszak, D.; Mazur, M.; Kaczmarek, D.; Domaradzki, J. Influence of doping with Co, Cu, Ce and Fe on structure and photocatalytic activity of TiO_2 nanoparticles. *Mater. Sci. Poland* **2017**, *35*, 725–732. [CrossRef]

23. Sahoo, S.; Arora, A.K.; Sridharan, V. Raman line shapes of optical phonons of different symmetries in anatase TiO_2 nanocrystals. *J. Phys. Chem. C* **2009**, *113*, 16927–16933. [CrossRef]

24. Su, C.Y.; Lin, H.C.; Lin, C.K. Fabrication and optical properties of Ti-doped $W_{18}O_{49}$ nanorods using a modified plasma-arc gas-condensation technique. *J. Vac. Sci. Technol. B* **2009**, *27*, 2170–2174. [CrossRef]

25. Yang, C.C.; Li, S. Size-dependent Raman red shifts of semiconductor nanocrystals. *J. Phys. Chem. B* **2008**, *112*, 14193–14197. [CrossRef] [PubMed]

26. Cappelli, I.; Fort, A.; Lo Grasso, A.; Panzardi, E.; Mugnaini, M.; Vignoli, V. RH sensing by means of TiO_2 nanoparticles: A comparison among different sensing techniques based on modeling and chemical/physical interpretation. *Chemosensors* **2020**, *8*, 89. [CrossRef]

27. Raji, P.; Binitha, H.S.; Kumar, K.B. Synthesis and humidity sensing properties of Sn-doped nano-TiO_2. *J. Nanotechnol.* **2011**, *2011*, 569036. [CrossRef]

28. Şaşmaz Kuru, T. Synthesis and investigation of structural, dielectric, impedance, conductivity and humidity sensing properties of Cr^{3+}-substituted Mg–Zn ferrite nanoparticle. *Appl. Phys. A* **2020**, *126*, 419. [CrossRef]

29. Gurlo, A.; Bârsan, N.; Oprea, A.; Sahm, M.; Sahm, T.; Weimar, U. An n- to p-type conductivity transition induced by oxygen adsorption on α-Fe2O3. *Appl. Phys. Lett.* **2004**, *85*, 2280. [CrossRef]

30. Sumets, M.; Dannangoda, G.C.; Kostyuchenko, A.; Ievlev, V.; Dybov, V.; Martirosyan, K.S. Temperature transition of p- to n-type conduction in the $LiNbO_3/Nb_2O_5$ polycrystalline films. *Mater. Chem. Phys.* **2017**, *191*, 35–44. [CrossRef]

31. Guo, L.; Wang, X.Q.; Zheng, X.T.; Yang, X.L.; Xu, F.J.; Tang, N.; Lu, L.W.; Ge, W.K.; Shen, B.; Dmowski, L.H.; et al. Revealing of the transition from n- to p-type conduction of InN:Mg by photoconductivity effect measurement. *Sci. Rep.* **2014**, *4*, 4371. [CrossRef]

32. Bohra, A.K.; Bhatt, R.; Singh, A.; Bhattacharya, S.; Basu, R.; Meshram, K.N.; Sarkar, S.K.; Bhatt, P.; Patro, P.K.; Aswal, D.K.; et al. Transition from n- to p-type conduction concomitant with enhancement of figure-of-merit in Pb doped bismuth telluride: Material to device development. *Mater. Des.* **2018**, *159*, 127–137. [CrossRef]

33. Pan, M.; Sheng, J.; Liu, J.; Shi, Z.; Jiu, L. Design and verification of humidity sensors based on magnesium oxide micro-arc oxidation film layers. *Sensors* **2020**, *20*, 1736. [CrossRef] [PubMed]

34. Barsan, N.; Grigorovici, R.; Ionescu, R.; Motronea, M.; Vancu, A. Mechanism of gas detection in polycrystalline thick film SnO_2 sensors. *Thin Solid Films* **1989**, *171*, 53–63. [CrossRef]